Uncovering the Timescales of Spin Reorientation in TbMn₆Sn₆

Sinéad A. Ryan^{1*}, Anya Grafov¹, Na Li¹, Hans T. Nembach^{2,3}, Justin M. Shaw⁴, Hari Bhandari⁵, Tika Kafle¹, Richa Sapkota¹, Henry C. Kapteyn^{1,6}, Nirmal J. Ghimire⁵, Margaret M. Murnane¹

¹JILA, University of Colorado Boulder, 440 UCB, Boulder, CO 80309, USA.

²Associate Physical Measurement Laboratory, National Institute of Standards and Technology, Boulder, CO 80305.

³Department of Physics, University of Colorado Boulder, Boulder, CO 80309, USA.

⁴Physical Measurement Laboratory, National Institute of Standards and Technology, Boulder, CO 80305.

⁵Department of Physics and Astronomy and Stavropolous Center for Complex Quantum Matter, 438

Nieuwland Science Hall, University of Notre Dame, Notre Dame, IN 46556 USA

⁶KMLabs Inc., Boulder, CO, USA

*Corresponding author. Email: sinead.ryan@colorado.edu

Abstract

TbMn₆Sn₆ is a ferrimagnetic material which exhibits a highly unusual phase transition near room temperature where spins remain collinear while the total magnetic moment rotates from out-of-plane to in-plane. The mechanisms underlying this phenomenon have been studied in the quasi-static limit and the reorientation has been attributed to the competing anisotropies of Tb and Mn, whose magnetic moments have very different temperature dependencies. In this work, we present the first measurement of the spin-reorientation transition in TbMn₆Sn₆. By probing very small signals with the transverse magneto-optical Kerr effect (TMOKE) at the Mn M-edge, we show that the re-orientation timescale spans from 12 ps to 24 ps, depending on the laser excitation fluence. We then verify these data with a simple model of spin precession with a temperature-dependent magnetocrystalline anisotropy field to show that the spin reorientation timescale is consistent with the reorientation being driven by very large anisotropies energies on approximately \approx meV scales. Promisingly, the model predicts a possibility of 180° reorientation of the out-of-plane moment over a range of excitation fluences. This could facilitate optically controlled magnetization switching between very stable ground states, which could have useful applications in spintronics or data storage.

Introduction

There has been a recent increase in interest in the field of ferrimagnetic spintronics¹, as well as ferrimagnetic spin reorientations, due to the potential application in stress-mediated magnetoelectric memory cells (MELRAMs)^{2,3}. A recent study⁴ of the kagome ferrimagnet TbMn₆Sn₆ (Tb166), has extensively investigated the nature of its spin reorientation transition at 309 K (T_{SR}). Manganese atoms form the interwoven stars of the Kagome net. The transition metal Manganese atoms are ferrimagnetically coupled with rare-Earth Terbium atoms. As the temperature is increased through T_{SR} , the magnetic moment rotates from out-of-plane to in-plane due to the competing anisotropies of the Tb and Mn magnetic sublattices. Tb166 may be particularly exciting for spintronic applications as the spin reorientation temperature is very near room temperature and, therefore, this transition could be readily accessible by gentle heating for a low power spintronic device. TbMn₆Sn₆ has also generated recent interest because of the observation that it can support non-trivial spin textures⁵ as well as other many-body physics effects arising from the interplay between the well separated Kagome layers of Mn atoms.

Spin reorientations have been studied for many years, yet are challenging to measure experimentally as they can be very fast (picosecond timescales). The first phenomenological model of spin reorientations due to temperature-dependent anisotropy was proposed in 1968⁶. The spin reorientation transition is a first-order phase transition, when the temperature is increased above T_{SR} , the magnetic moments spontaneously rotate from out-of-plane to in-plane. The ferrimagnetism is governed by an indirect exchange between Mn moments mediated by anti-aligned Tb moments. The spin reorientation is thought to arise due to the competing anisotropy of the Tb, which has easy-axis anisotropy, and the Mn, which has easy-plane anisotropy⁴. As the sample is heated towards the Curie temperature, T_{C} , the Tb moment drops off more rapidly than the Mn moment. This is because the ferromagnetic indirect Mn-Mn exchange produces a stronger molecular field than the molecular field that is experienced by the Tb moments. As a result, at temperatures ≈ 100 K below the Curie temperature (i.e. T_{SR}), the Mn anisotropy out-competes the Tb anisotropy and this spontaneously pulls the magnetic moment in-plane, while preserving the ferrimagnetic alignment between the Tb and Mn spins.

In this study, we make the first measurements of the intrinsic timescale of the spin reorientation transition in TbMn₆Sn₆. We also compare these data with a simple model of spin precession with the aim to further our understanding of spin-reorientation transitions for spintronic applications. By probing very small TMOKE signals at the Mn M-edge, we can make extremely sensitive magnetic measurements of the Mn sublattice and show that the re-orientation timescale spans from 12 to 24 ps, depending on the laser excitation fluence. This timescale is consistent with the reorientation being driven by very large anisotropies energies, on the \approx meV scale, and is consistent with what is expected for a rare-Earth transition metal alloy. We verify the spin reorientation timescale by implementing the Landau-Lifshitz equation with a temperature-dependent magnetocrystalline anisotropy field. Promisingly, the model predicts a possibility of 180° reorientation of the out-of-plane moment over a range of excitation fluences. This could facilitate optically controlled magnetization switching between very stable ground states, which could have useful applications in spintronics or data storage.

In addition to measurements of the spin reorientation, we will also investigate the laser-induced ultrafast demagnetization of TbMn₆Sn₆, which proceeds on a timescale of ≈1ps – which is an order of magnitude fast than the spin reorientation. Past research measured very fast demagnetization rates in 3d transition metals (TMs) of a few 100's fs^{7,8}. However, 4f rare-Earth magnets (RE) demagnetize at a much slower rate in a two-step process^{8,9}. For example, both Gd and Tb initially demagnetize at a rate of 750 fs followed by a much slower secondary demagnetization with a rate of 40 ps for Gd and 8 ps for Tb⁹ respectively. However, demagnetization times of the RE magnetic sublattice in RE-TM alloys can be as fast as those of pure TMs¹⁰. Several studies have investigated the ultrafast demagnetization of multi-element alloys containing both RE and TM magnetic sublattices 10-12. It has been proposed that the ferrimagnetic alignment of the magnetic sublattices in RE-TM alloys allows spin angular moment to be transferred between the 3d and 5d orbitals of TM and RE respectively leading to a faster demagnetization of both the RE and TM¹³. Due to this mechanism, demagnetization times for RE-TM alloys were found to be fastest, when the excitation brings the system in the vicinity of the compensation temperature (T_{comp}), where the RE and TM moments are equal and opposite, rather than the Curie temperature $(T_c)^{10}$ - where spindisorder would be maximized in the quasi-static case. In TbMn₆Sn₆, there is no compensation temperature. This is because the Mn sublattice always carries a higher moment⁴, due to the 6:1 ratio of Mn atoms to Tb atoms (despite Tb carrying a larger magnetic moment per atom). Nevertheless, we may expect demagnetization times to be quite fast compared to pure Tb.

Measurements of time-dependent sample magnetism were performed using the X-MATTER beamline 14 in Boulder. A Ti: Sapphire regenerative amplifier was used to drive high harmonic generation (HHG) in a neon gas medium. This produced a comb of harmonic probing energies in the extreme ultraviolet (EUV) range. Energies in the HHG comb were spectrally dispersed using a diffraction grating and the intensities were recorded on a CCD chip. The EUV light resonantly probed the in-plane Mn moment at the M-edge (47.2 eV) using the transverse magneto-optical Kerr effect (TMOKE). Sample dynamics were excited using pulses from the Ti: Sapphire laser with a 780 nm central wavelength, 40 fs duration pump laser and a 5 kHz repetition rate. The pump spot had $1/e^2$ radii of 316 μ m by 535 μ m. The probe spot had a $1/e^2$ radius of approximately 40 μ m. No active heating or cooling was applied to the sample. However, larger pump fluences resulted in higher baseline sample temperatures due to the undissipated heat from the pump laser.

The magnitude of the in-plane Mn magnetic moment was determined by calculating the TMOKE magnetic asymmetry which was based on differential intensity measurements with applied fields of 185 mT \pm 15 mT in-plane and a p-polarized incident beam at near-Brewster:

$$A(t) = \frac{I_{+}(t) - I_{-}(t)}{I_{+}(t) + I_{-}(t)} \tag{1}$$

Where A(t) is the magnetic asymmetry signal, $I_+(t)$ is the time-dependent reflectivity of the sample with an applied field of +185 mT, and $I_-(t)$, is the time-dependent reflectivity of the sample with an applied field of - 185 mT. More details of the beamline design and magnetic asymmetry measurement scheme appear in Johnsen $et\ al.^{14}$

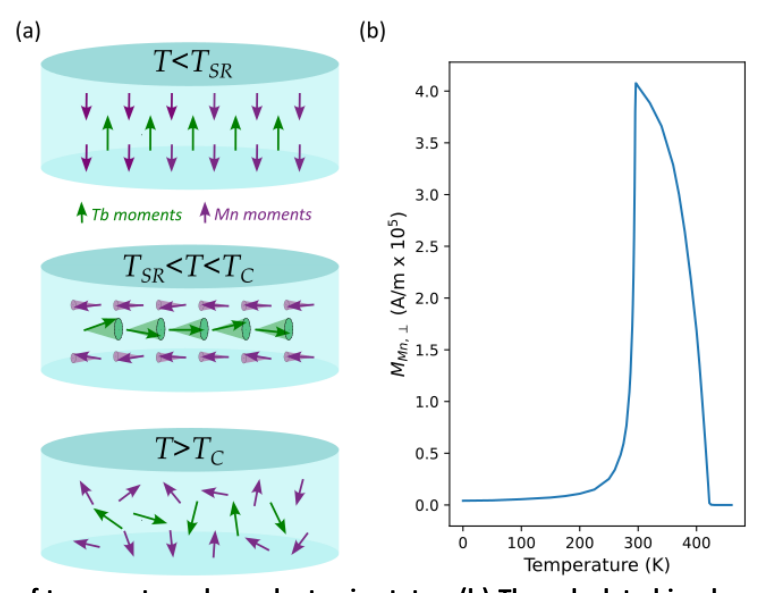


Figure 1. (a) Schematic of temperature-dependent spin states. (b) The calculated in-plane projection of the Mn moment vs. temperature with an in-plane applied field of +185 mT (to match experimental value). (a) There is an out-of-plane ferrimagnetic alignment between Mn and Tb moments below T_{SR} . Above T_{SR} , but below T_{C} , there is an in-plane ferrimagnetic alignment of Mn and Tb moments. As the temperature approaches T_{C} , spin-disorder increases due to thermal fluctuations and this is represented with cones showing canted spins. The Tb disorder is depicted as being larger because the Tb moment drops off more rapidly than Mn as temperature is increased. Above T_{C} , the spin orientation is fully randomized. (b) This subfigure was produced by combining anisotropy data from Jones *et al.*⁴ and magnetic moment data from El-Idrissi *et al.*¹⁵ The in-plane Mn moment is maximized just above the spin reorientation temperature. The signal is small or zero below T_{SR} and above T_{C} .

Results

Following ultrafast laser excitation, it is common to use a phenomenological three-temperature model in which the electrons, spins, and lattices each have their own distinct temperatures (they have not yet had time to thermalize with each other). When describing the Tb166 temperature, unless otherwise specified, we concern ourselves with the spin-system temperature specifically (since the spin reorientation transition is governed by the temperature-dependent behavior of the spin system). On timescales longer than a few ps^{16,17}, this is no longer an issue as the three systems (electron, spin lattice) have had time to equilibrate and reach a unified temperature distribution. The time-dependent spin bath temperature is explored in more detail in the modelling section.

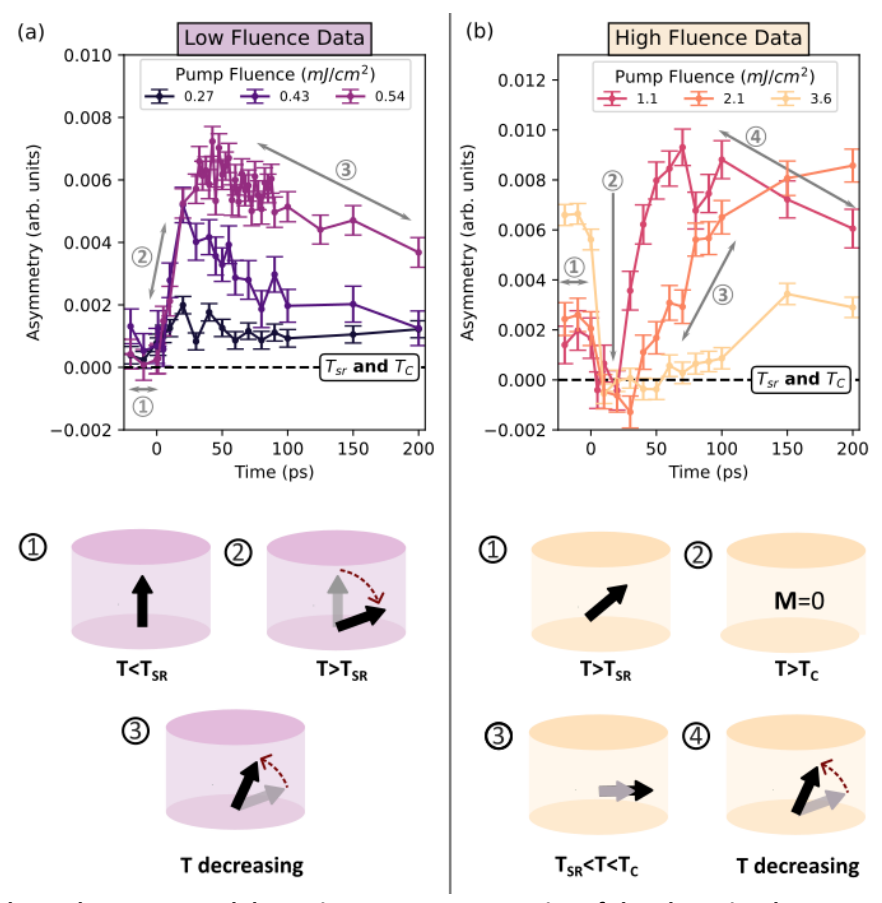


Figure 2. Fluence-dependent measured dynamic TMOKE asymmetries of the Tb166 in-plane Mn moment probed at 46.2 ± 0.2 eV. The measured magnetic asymmetry with an applied field of 185 ± 15 mT with (a) low pump fluences and (b) the high pump fluences. The low and high fluence data are described with 3 and 4 step processes respectively. These are included as an annotation to the experimental data as well as being shown as a cartoon in the lower section of the figure. Below T_{SR} and above T_C the signal is approximately zero because in both these cases there is no in-plane component to the magnetization. This threshold is depicted by the black dotted line.

Fig. 1(a) depicts the temperature-dependent spin-alignment in Tb166 in three specific temperature regimes. The measured TMOKE signal comes from the in-plane Mn moment. Therefore, to help interpret the experimental results, in Fig. 1(b), we calculate the in-plane Mn moment with temperature. This figure reveals, if the measured TMOKE signal has a value of zero or near-zero, this indicates that the sample temperature is either in the low temperature regime, below T_{SR} , or the high temperature regime above

 T_c . In the first instance, the total moment is still large but points out-of-plane, and in the second instance, the total moment is zero. Fig. 1(b) was generated according to the model as described in the modelling section.

Fig. 2 shows the time-dependent magnetic asymmetry signal for a range of different pump fluences. A normalization factor was applied to each curve, which is explained in more detail in the SM. Data in Figs. 2, 3 & 7 are measured with a harmonic probing energy of 46.2 eV ± 0.2 eV which is the 29th harmonic of the driving laser. This harmonic was most resonant with the Mn M-edge (47.2 eV)¹⁸, and therefore, had the strongest TMOKE signal. While measurements at this energy are sensitive to the Mn behavior specifically, the Mn and Tb moments are expected to remain collinear⁴ since ferrimagnetic orders persists even above the reorientation transition.

To understand the fluence-dependent behavior, the TMOKE results are divided in Fig. 2(a), the low fluence regime and Fig. 2(b), the high fluence regime. The low fluence behavior can be broken down into three key steps: first (pre-time-zero), the sample temperature has not exceeded T_{SR} and the magnetization is mostly out of plane, which means the measured in-plane EUV MOKE signal is near zero. Next (after ultrafast excitation by the pump laser pulse partially sends the spin system through the reorientation transition), the signal increases with time as spins rotate in-plane. The amplitude of the TMOKE signal scales with the fluence applied, because when the sample is pumped harder, it goes through the spin reorientation transition more completely, i.e. a greater portion of the sample is magnetized in-plane. Finally (approximately 30-200 ps after excitation), the sample cools as heat is gradually dissipated to unpumped regions of the sample, the epoxy, and the sample mounting plate. The TMOKE signal gradually reduces as the sample cools below T_{SR} and the spins start to reorient back out-of-plane.

Fig. 2(b) depicts the high fluence data, which can be broken down into four key steps. In this case, the minimum sample temperature is higher than for the low fluence measurements due to a larger incident pump power (which heats the sample since it is not actively cooled). This combined with the 5 kHz repetition rate of the laser does not provide sufficient time between pulses to cool the sample below T_{SR} . Therefore, a larger fraction of the Mn magnetic moment is initially in-plane. Next, after laser excitation, the sample demagnetizes when the temperature of the electron-spin system exceeds the Curie temperature. The sample then cools due to coupling to phonons and heat transport into the bulk, and remagnetizes in-plane as it transitions back to temperatures below T_C but above T_{SR} . The largest fluence (3.6 mJ/cm²) takes the longest time to recover and the smallest fluence (1.1 mJ/cm²) takes the least time to recover. Finally, the sample cools further, and as it approaches T_{SR} , it starts to lose its in-plane moment in favor of an out-of-plane moment. Therefore, the signal decreases. Within the measurement window of 200 ps, this signal decrease only occurs in 1.1 mJ/cm² data. However, we can expect the other two curves (2.1 mJ/cm² and 3.6 mJ/cm²) to exhibit the same behavior on longer timescales. In the 3.6 mJ/cm² and 2.1 mJ/cm² data, after the initial excitation, the sample and thus the spin bath temperature remains above T_{SR} until the end of the scan at 200 ps. In the high fluence regime, the dynamics are dominated by the timescale of the sample re-magnetizing in-plane as it dissipates heat (steps 2 & 3 in Fig. 2(b)). Therefore, the timescales of recovery come from the rate of heat dissipation from the probed region of the sample.

In the $0.27 \text{ mJ/cm}^2 - 0.54 \text{ mJ/cm}^2$ data (low fluence), the spin reorientation transition is addressed. The initial rise time is fitted in Fig. 3 and represents the spin reorientation response to a rapid anisotropy change through impulsive heating. The slow decay from $\approx 30\text{-}200 \text{ ps}$, represents the spin temperature relaxing which drives the spin orientation back out-of-plane.

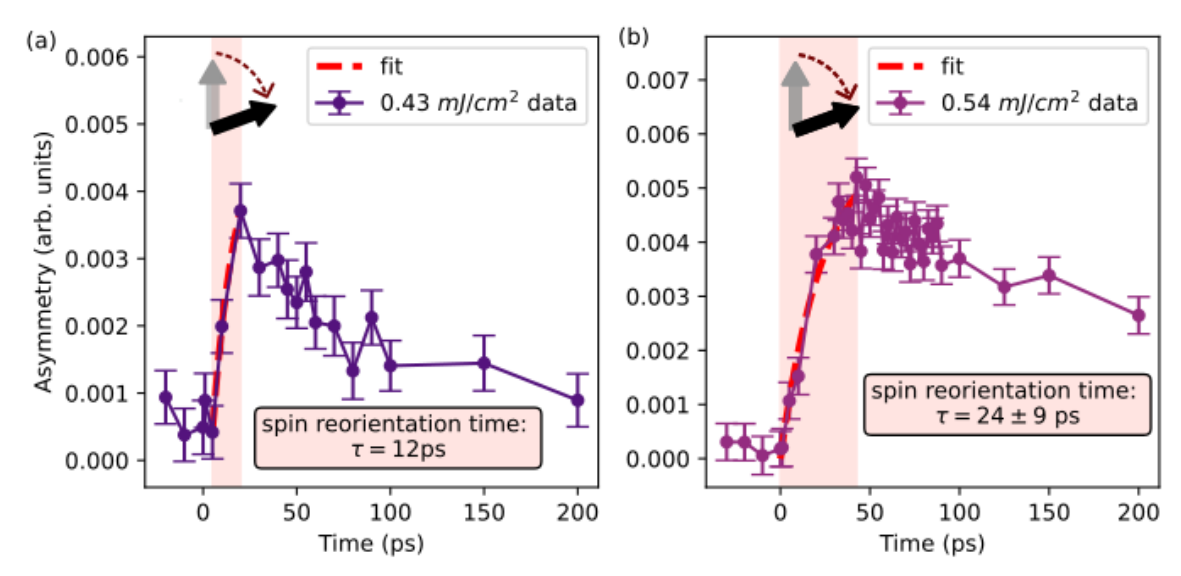


Figure 3. Exponential fit of spin reorientation timescale. Measured with a harmonic probing energy of 46.2 eV \pm 0.2 eV. The rise time of the spin reorientation at (a) 0.43 mJ/cm² and (b) 0.54 mJ/cm² were fitted using Eq. 2.

In Fig. 3, we fit the low fluence data from Fig. 2 (a), with an exponential function of the form:

$$A(t) = C \left[1 - e^{\frac{-(t - t_0)}{\tau}} \right] \tag{2}$$

where A(t) is the measured magnetic asymmetry signal, C is the amplitude, t is time, t_0 is an offset to account for any differences between the time-zero as defined in the figure and the time-zero determined by the fit. τ is the time-constant of the exponential. For the fitting process, the data was truncated to include only the exponential rise (starting from lowest point and continuing to the highest point). The 0.27 mJ/cm² data was not included as the signal-to-noise ratio was too poor to perform the fit. For the 0.43 mJ/cm² data, a time-constant of 12 ps was obtained. However, as only three data points were included in the fit, a confidence interval for the fitting parameters could not be established. For the 0.54 mJ/cm² data, the fitted time-constant was 24 ps \pm 9 ps. Therefore, the spin reorientation timescale is very fast, \approx 20 ps. We attribute this to the very large anisotropy energies present in Tb166.

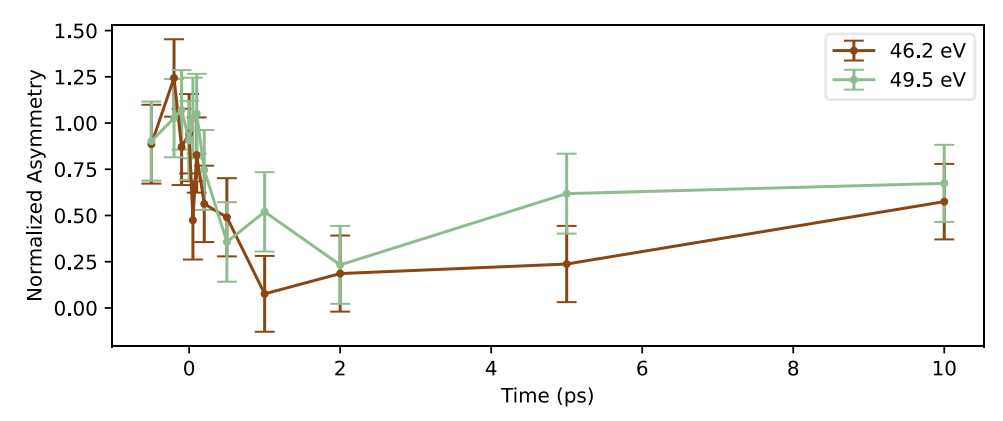


Figure 4. Demagnetization of Tb166 with 1.1 mJ/cm² pump fluence. Dynamic asymmetries from -0.5 to 10 ps as measured with harmonic probing energies centered at 46.2 eV \pm 0.2 eV and 49.5 eV \pm 0.2 eV. Demagnetization is an order of magnitude faster than the spin reorientation timescale.

In Fig. 4, a measurement of sample demagnetization with a 1.1 mJ/cm² pump fluence is depicted with additional data points taken to achieve good time resolution in the first 10 ps. The average pre-time-zero signal is normalized to one. Two different probing energies near the Mn M-edge are given (46.2 eV and 49.5 eV) and they each show similar dynamics. The 49.5 eV data is not presented in the previous figures as the signal-to-noise ratio was relatively poor. The timescale for demagnetization is approximately 1 ps, which is approximately 20 times faster than the reorientation timescale. This demagnetization timescale is in keeping with what is expected for a RE-TM alloy as discussed in the introduction.

Modelling

To model the spin reorientation transition, we construct a time-dependent effective field, $\mathbf{H}_{\mathbf{eff}}(t)$, which will act on the sample's magnetization unit vector, $\mathbf{m}(t)$, in the Landau-Lifshitz equation:

$$\mathbf{H}_{\text{eff}}(t) = \mathbf{H}_{\text{annl}} + \mathbf{H}_{\text{demag}}(t) + \mathbf{H}_{\text{anis}}(t) \tag{3}$$

where $\mathbf{H_{appl}}$ is a constant applied field in the +x direction with a value of 185 mT. The demagnetizing field, $\mathbf{H_{demag}}(t)$, is much weaker than the anisotropy field and does not have a large impact on the dynamics. The expression for $\mathbf{H_{demag}}(t)$ is given in the Supplementary Materials. $\mathbf{H_{anis}}(t)$ acts along the z-axis and is described in more detail in the Supplementary Materials:

$$\mathbf{H_{anis}}(t) = m_z(t) \left(\frac{MAE_{Tb} \left(T_{spin}(t) \right) + 6MAE_{Mn} \left(T_{spin}(t) \right)}{\mu_0 M_s \left(T_{spin}(t) \right)} \right) \hat{\mathbf{z}}$$
(4)

where $m_z(t)$ is the projection of $\mathbf{m}(t)$ along the z-axis, and $M_s\left(T_{\mathrm{spin}}(t)\right)$ is the saturation magnetization, previously determined using neutron scattering¹⁵, as a function of the instantaneous spin bath temperature, T_{spin} , which changes with time, t. MAE_{Mn} and MAE_{Tb} are the anisotropy energies of the Tb and Mn sublattices given with temperature-dependence by Jones $et~al.^4$ The usual factor of two which would be applied in converting from anisotropy energy to anisotropy field has been omitted due to the definition of MAE by Jones $et~al.^4$ A factor of 6 is applied to the Mn term to account for the six Mn atoms per unit cell.

Writing the Landau-Lifshitz equation in full vector form, we then obtain:

$$\frac{d\mathbf{m}}{dt} = -\gamma \left(\mathbf{m} \times \left(\mathbf{H}_{\mathbf{demag}}(t) + \begin{bmatrix} H_{\mathrm{appl}} \\ 0 \\ H_{\mathrm{anis}}(t) \end{bmatrix} \right) \right) - \frac{\alpha\gamma}{m} \left(\mathbf{m} \times \mathbf{m} \times \left(\mathbf{H}_{\mathbf{demag}}(t) + \begin{bmatrix} H_{\mathrm{appl}} \\ 0 \\ H_{\mathrm{anis}}(t) \end{bmatrix} \right) \right)$$
(5)

where α is the damping factor. The temperature of the sample magnetization, i.e. the spin bath temperature, is estimated based on three time-dependent exponential functions:

$$T_{\text{spin}}(t) = T_0 + A_1 \left(1 - e^{-t/\tau_{\text{rise}}} \right) - A_2 \left(1 - e^{-t/\tau_{\text{decay1}}} \right) - A_3 \left(1 - e^{-t/\tau_{\text{decay2}}} \right)$$
 (6)

where T_0 is the initial temperature of the sample prior to pump excitation. The amplitude A_1 represents the heating of the spin bath from the pump laser. The first timescale, $\tau_{\rm rise}$, comes from the rate of energy transfer from the electrons (which are directly excited by the laser pulse) to the spin bath. This rate of energy transfer to the spin bath is estimated to be 1 ps, based on the rate of ultrafast demagnetization of

this sample, as shown in Fig. 4. The second term, whose magnitude is given by A_2 , represents the spin-lattice thermalization time. The spin-lattice thermalization reduces the spin bath temperature on a short timescale. Based on typical values for the three-temperature model, this timescale (τ_{decay1}) is roughly estimated at 3 ps based on typical timescales^{16,17}. On a longer timescale, the spin-bath temperature is further reduced due to thermal diffusion. This is represented in the final term with amplitude A_3 . The experimental TMOKE signals decay on timescales similar to the total scan time, i.e. 200 ps. Therefore, τ_{decay2} time is estimated to be 200 ps. While this thermal model is a relatively simplistic interpretation of the evolving temperatures and heat capacities of the system, it is sufficient for recreating some of the characteristic behavior of the sample.

In the model, spin reorientation occurs at a temperature of 300 K with no applied field. This is based on the equation for temperature-dependent anisotropies given by Jones et al.4 and temperature-dependent spin moments from El-Idrissi et al. 15 This is close to the literature value for spin reorientation of 309 K⁴, although the model is slightly on the lower side of the literature value. After including the applied in-plane field of 185 mT, the spin reorientation occurs in the model at even lower temperatures. The in-plane moment exceeds the out-of-plane at temperatures as low as 295 K. In the measured data, with an applied field of 185 mT, the pre-time-zero in-plane moment remains relatively small for all fluences except for the highest, 3.4 mJ/cm², Fig. 2. This implies that the experimental spin-reorientation occurs in the range of 315 K to 319 K, e.g. up to 10 K higher than the literature value (even with the applied field of 185 mT). The measured sample temperature may not be exactly the real sample temperature because of the location of the temperature probe. This is discussed in more detail in the *Materials and Methods* section. Since the spin-reorientation temperature is lower in the model, and higher in the experiment, we use a lower initial temperature in the model than the temperatures that were measured in the experiment. By beginning the model at a lower temperature, we can still investigate the dynamics of an ultrafast excitation through T_{SR} rather than using the measured temperature which would put the sample above T_{SR} in all cases.

The time-dependent LL equation, Eq. 5, is solved using MATLAB's ode45 which is a built-in non-stiff differential equation solver. To obtain the final comparison with experiment, the x-component of the time-dependent magnetization vector, $m_{\chi}(t)$, obtained from the time-evolution of Eq. 5, is multiplied by the calculated temperature-dependent Mn magnetization. This aligns the simulation with the experiment since the TMOKE measurement only measures the x-component of the Mn moment.

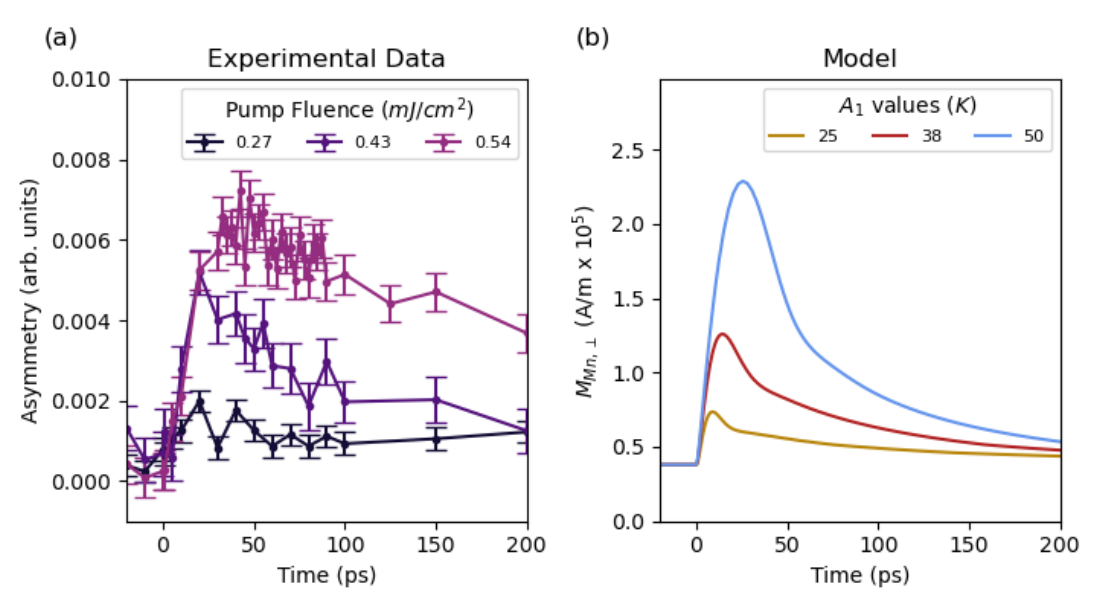


Figure 5. A low fluence dynamic model of Tb166. The modeling is based on the temperature profile described by Eq. 6. Experimental data probed with a harmonic energy of 46.2 eV \pm 0.2 eV is presented for comparison in (a). (b) Explores effects of changing the initial heating amplitude A_1 .

The results of the low fluence simulation are shown in Fig. 5. The effect of changing the incident fluence is shown experimentally in Fig. 5(a), and in simulation in Fig. 5(b). The simulated fluence is determined by the amplitude of the applied spin temperature increase, parameter A_1 in Eq. 6. Unless otherwise specified the parameters used were as follows: $T_0 = 270$ K, $A_2 = 1/2$ A_1 , $A_3 = 1/2$ A_1 , $\tau_{rise} = 1$ ps, $\tau_{decay1} = 3$ ps, $\tau_{decay2} = 200$ ps, and $\alpha = 1$. There is good agreement between the experimental trends and the shapes of the simulated figures across a wide range of temperature model parameters- this is explored in more details in the Supplementary Materials. The real temperature profile of the sample may be quite complex. There are many different timescales for heat transport in the sample: spin-electron thermalization, spin-lattice thermalization, sample-epoxy thermalization, epoxy-mount thermalization etc. Furthermore, the heat capacity of each of these systems in not linear in temperature. Nonetheless, the shape and timescale of the low fluence spin reorientation is effectively reproduced with this simple model.

In the simulations in Fig. 5, a critical damping value of $\alpha=1$ was used. With a more physical value of α (e.g. 0.01 to 0.1), as depicted in Fig. S1 (supplemental materials, SM), very large oscillations dominate. However, in the experimental data we do not see these large precessions. This lack of clear oscillations in the data can be explained by a non-uniform excitation of the Tb166 spin system. Not all probed parts of the sample experience identical excitation amplitudes due to non-uniform laser heating and sample inhomogeneities. Therefore, we cannot expect the probe to measure an in-phase bulk precessional motion since the temperature-dependent direction and strength of the anisotropy field will not be uniform in the probed region. By applying a damping factor of $\alpha=1$, we can see the underlying dynamics without the overriding precessional motion. This allows us to compare the model with the experimental results.

We fit the initial rise of the magnetization curves in Fig 5. (b) to obtain the model's spin reorientation timescales. We obtain very good agreement with the experimentally obtained timescales. For the three heating amplitudes ($A_1 = 25 \text{ K}$, 38 K, 50 K) exponential rise times of: 8.3 ps \pm 1 ps, 10.9 ps \pm 1 ps, and 15.3

ps \pm 1 ps were obtained. The first two values are close to the 0.42 mJ/cm² experimental fit of 12 ps, and the third value falls inside the experimental error bars (24 ps \pm 9 ps) for the 0.54 mJ/cm² data.

To prove that model is measuring an intrinsic timescale, rather than being dependent on some specific of temperature model parameters in Eq. 6, we also tested how the model responded to a step-function increase in temperature (i.e. temperature was instantaneously increased with no decays). Using the maximum and minimum temperatures from Fig. 5(b) for the step-function, we obtained fits of 4.3 ps \pm 0.1 ps, 14.7 ps \pm 0.4 ps and 21.9 ps \pm 0.2 ps for the three cases. The agreement with experimental timescales (e.g. 12 ps, 24 ps \pm 9 ps) is rather remarkable when we consider that the only free parameters in the step-function model are the initial and final temperature as well as the damping term α (which is set to 1). The step-function model is described in more details in the SM.

When we consider the precession of spins in a magnetic field, the intrinsic timescale can be best understood through the energy-time correlation¹⁹:

$$t \sim h/E. \tag{7}$$

This equation links the cycle time, t, to its characteristic energy, E. From this relationship, we derive that for an energy of 1 meV, we should expect a cycle time of 4 ps. Therefore, for the meV energy scale of the Tb166 anisotropy, we should expect an intrinsic ps timescales as confirmed experimentally and in the model. The large anisotropies of the Tb166 facilitates the fast reorientation (10's of ps timescale).

In Fig. 6, we explore the 3-dimensional nature of the spin reorientation and increased sample heating is investigated. The initial temperature is 270 K, meaning that the spin is orientated out-of-plane, i.e. on the z-axis. The applied field of 185 mT in the +x direction means that the initial state has a small +x component, i.e. it is slightly canted from the z-axis. The sample temperature is increased with the three-exponential model. In this figure, slightly higher fluences are investigated compared to Fig. 5.

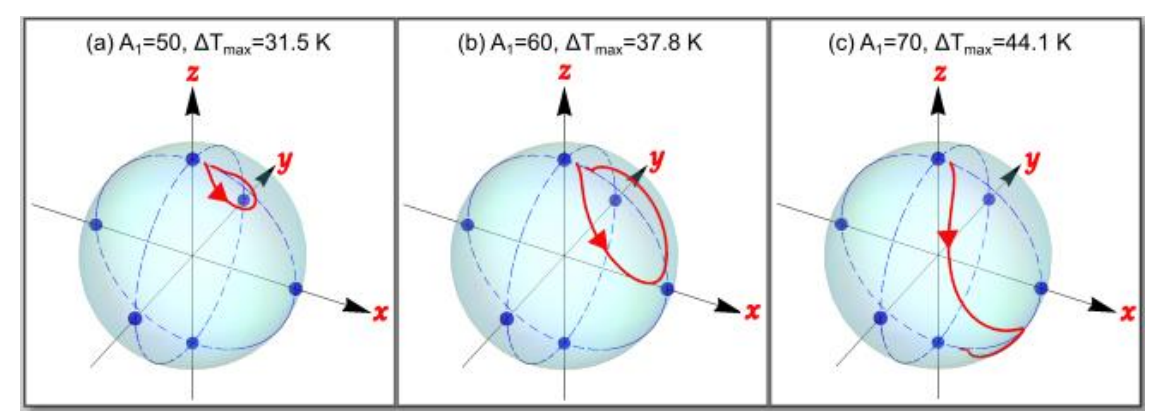


Figure 6. A 3-dimensional depiction of the dynamics of the Tb166 magnetization vector. The path of the magnetization unit vector is traced out in red over the first 200 ps of the dynamics. The sample plane is oriented in x-y. The z-axis is the out-of-plane direction. Three different magnitudes of induced temperature changes are plotted.

In Fig. 6(a) $A_1 = 50$ K, and 6(b) $A_1 = 60$ K, the magnetization vector traces out a small circle as the spin reorients then cools towards its original orientation. In (c) $A_1 = 70$ K the reorientation overshoots the x-y plane and the sample cools towards the -z direction. This occurs when the torque from the spin-reorientation causes the magnetization vector to overshoot the x-y plane, creating a small negative z component. If the sample cools below T_{SR} while there is a negative z component, then negative z will be preferable over positive z (since both poles are energetically equivalent). The model shows this reversal

when A_1 (heating amplitude) is anywhere in the range of 61-90 K. This mechanism for laser-induced ultrafast magnetization switching has not been previously proposed.

We note that for more physical damping factors, i.e. $\alpha=0.1$ or 0.01, this behavior still occurs but the final state is very sensitive to the exact temperature profile and the exact value of the damping. This is because the precessional motion can change the sign of the z-component and therefore send the system towards a different energy minimum.

Unfortunately, our measurement technique is not sensitive +z vs. -z alignments. We have no way of determining the initial or final z-axis direction in our experimental as both directions are energetically equivalent and the initial z-direction does not affect the x-projected dynamics that are measured.

The potential for a 180° reorientation of Fig. 6(c) opens up the possibility that this material could be switched by ultrafast pulses between two exceedingly stable ground state configurations without requiring very large laser fluences. The anisotropy barrier at room temperature is much larger than transition metal alloys traditionally used in magnetic recording. Furthermore, Tb166 only requires a small amount of heating to reach T_{SR} , compared to approaching the Curie temperature in more conventional ultrafast magnetic switching. However, Tb166 may not support the small domains required for practical data storage applications and precessional motion may make the final state difficult to predict.

Discussion

We note that the LL equation, Eq. 5, is not accurate when materials are near their Curie temperature since it does account for changes in magnetic damping near the Curie point or a magnetization magnitude which changes with temperature²⁰. To overcome this, a microscopic Landau-Lifshitz-Bloch (LLB) equation description was developed by Lyberatos and Guslienko²¹ with the intention of describing magnetic writing of nanoparticles subject to pulsed laser heating in HAMR hard drives. This implementation of the LLB equation is beyond the scope of this work. However, we can avoid this limitation by confining the simulations and analysis to temperatures that are at least 100 K below T_C , which includes the regime where the spin reorientation occurs. Modeling of the high fluence results is discussed in brief detail in the Supplementary Materials.

By measuring very small TMOKE signals at the Mn M-edge, we are able to uncover the ultrafast dynamics of spin reorientation in TbMn₆Sn₆ for the very first time. The ultrafast demagnetization proceeds on a timescale of about 1 ps. This is consistent with what we expect for a RE-TM alloy. The spin reorientation occurs on a timescale of \approx 20 ps. This timescale is consistent with the reorientation being driven by very large anisotropies energies, meV scale. We note that the spin reorientation timescale (\approx 20 ps) is an order of magnitude slower than the ultrafast demagnetization (\approx 1 ps). We observe distinct behavior in key regimes of high and low fluence pumping. The high fluence timescales are governed by heat dissipation at temperatures around T_{C} . The early timescales of low fluence data are governed by impulsive anisotropy changes. The later timescales are governed by heat dissipation at temperatures around T_{SR} . We verify the spin reorientation timescale by implementing the LL equation with a temperature-dependent magnetocrystalline anisotropy field.

The low fluence model successfully replicated the measured ≈20 ps spin-reorientation timescale both with a trial temperature profile and with a step-function temperature profile with few free parameters. Promisingly, the model predicts a 180° reorientation of the out-of-plane moment over a range of excitation fluences. This could facilitate optically controlled magnetization switching between very stable

ground states, which could have useful applications in spintronics or data storage. However, this result still needs to be verified experimentally.

Materials and Methods

Single crystals of TbMn₆Sn₆ were grown by self-flux methods as described by Jones *et al.*⁴ The magnetic asymmetries measured on this sample were, approximately, 10 - 100 times smaller than many typical samples conventionally measured with EUV TMOKE (e.g. Fe, Ni, Co, Py, etc.). These measurements were made possible by the excellent stability of the X-MATTER beamline¹⁴.

The sample was mounted on a 0.5 mm thick sapphire plate using a conductive silver epoxy (EPO-TEK® H20S). No active heating or cooling systems were applied to the sample. Sample temperatures were recorded using an in-vacuum thermocouple wire mounted on the back of the sapphire sample plate. The sample was subject to an in-plane applied field generated by an out-of-vacuum GMW 5201 projection field electromagnet with the maximal possible field strength of 185 ± 15 mT. The in-plane applied field was maximized to encourage the reorientation transition. The electromagnet was water cooled but still reached temperatures exceeding 40 °C during use. The sample was heated to above room temperature by thermal radiation from the electromagnet (situated behind the sample) and the pump laser (incident on the front of the sample). For each measurement, we allowed the sample to the thermalize for approximately 1 hr with the same electromagnet currents and laser pump fluences used in the experiment in order for the sample to reach a stable baseline temperature before data was taken. The electromagnet alone heated the sample to approximately 18 K above room temperature (≈310 K). The temperature rise induced by the pump laser was highly fluence-dependent. Measured sample temperatures varied from as high as ≈319 K for the highest fluence (3.6 mJ/cm²) to ≈311 K for the lowest fluence (0.27 mJ/cm²), Fig. 7. There was a small amount of ongoing thermalization that continued to increase the sample temperature throughout the scan after the 1 hr thermalization period. For this reason, we measured the temperature at the beginning (slightly lower temperature) and end of the scan (slightly higher temperature). These high and low temperature set the upper and lower bounds of the bars in Fig. 7. Heating from the EUV probe is negligible.

Statistical Analysis

Experimental time points were measured in a random order to minimize systematic errors from sample damage. An additional normalization factor was applied also mitigate sample damage effects and is explained in more detail in the Supplementary Materials. The error bars on the experimental data represent the standard deviation of repeated measurements and the data points are given by the arithmetic mean. Both the data and its error bars are multiplied by the normalization factor.

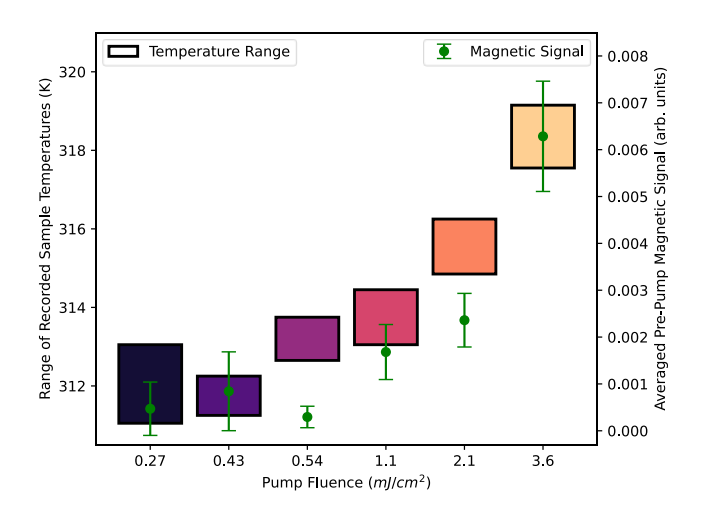


Figure 7. The relationship between static (pre-pump) magnetic signal and recorded sample temperature. The magnetic asymmetry signals at a probe energy of 46.2 ± 0.2 eV (green data points with error bars) were calculated by averaging the pre-pump-excitation data ($t \le 0$). As there were only 3- or 4-times points where $t \le 0$, in the dynamic measurements (Fig. 2), a student t-value weighting was multiplied by the standard error to obtain the error bars shown. The temperature ranges (solid color bars) indicate the maximum and minimum temperatures recorded by the temperature probe during the scan.

Acknowledgements

The authors acknowledge Igor I. Mazin for insightful discussion. The JILA authors gratefully acknowledge support from a Department of Energy Office of Basic Energy Sciences X-Ray Scattering Program under Award No. DE-SC0002002 (S.A.R., A.G., N.L., T.K., R.S., H.C.K., M.M.M.) and an NSF GRP (A.G.). N.J.G and H.B. acknowledge the support from the National Science Foundation (NSF) CAREER award DMR- 2343536.

Author Contributions: S.A.R., A.G., N.L., T.K. R.S., H.C.K. and M.M.M. conceived and conducted the experiments, and analyzed the experimental data. J.M.S. and H.N. advised on the theoretical calculations performed by S.A.R.. The sample was grown and characterized by H.B. and N.J.G.. All authors contributed to writing the manuscript.

Competing Interests: H.C.K. and M.M.M. have a financial interest in a laser company, KMLabs, that produces the lasers and HHG sources used in this work. H.C.K. is partially employed by KMLabs. All other authors declare they have no competing interests.

Certain commercial equipment, instruments, or materials are identified in this paper in order to specify the experimental procedure adequately. Such identification is not intended to imply recommendation or endorsement by the National Institute of Standards and Technology, nor is it intended to imply that the materials or equipment identified are necessarily the best available for the purpose

References

1. Kim, S. K. et al. Ferrimagnetic spintronics. Nat. Mater. 21, 24–34 (2022).

- 2. Ovcharenko, S. *et al.* Photoinduced spin dynamics in a uniaxial intermetallic heterostructure TbCo₂/FeCo. *Sci. Rep.* **10**, 15785 (2020).
- 3. Klimov, A. *et al.* Magnetoelectric write and read operations in a stress-mediated multiferroic memory cell. *Appl. Phys. Lett.* **110**, 222401 (2017).
- 4. Jones, D. C. *et al.* Origin of spin reorientation and intrinsic anomalous Hall effect in the kagome ferrimagnet TbMn₆Sn₆. Preprint at https://doi.org/10.48550/arXiv.2203.17246 (2022).
- 5. Li, Z. *et al.* Discovery of Topological Magnetic Textures near Room Temperature in Quantum Magnet TbMn6Sn6. *Adv. Mater.* **35**, 2211164 (2023).
- 6. Horner, H. & Varma, C. M. Nature of Spin-Reorientation Transitions. *Phys. Rev. Lett.* **20**, 845–846 (1968).
- 7. Beaurepaire, E., Merle, J.-C., Daunois, A. & Bigot, J.-Y. Ultrafast Spin Dynamics in Ferromagnetic Nickel. *Phys. Rev. Lett.* **76**, 4250–4253 (1996).
- 8. Koopmans, B. *et al.* Explaining the paradoxical diversity of ultrafast laser-induced demagnetization.

 Nat. Mater. 9, 259–265 (2010).
- Wietstruk, M. et al. Hot-Electron-Driven Enhancement of Spin-Lattice Coupling in Gd and Tb 4f
 Ferromagnets Observed by Femtosecond X-Ray Magnetic Circular Dichroism. Phys. Rev. Lett. 106, 127401 (2011).
- 10. López-Flores, V. *et al.* Role of critical spin fluctuations in ultrafast demagnetization of transitionmetal rare-earth alloys. *Phys. Rev. B* **87**, 214412 (2013).
- 11. Mentink, J. H. *et al.* Ultrafast Spin Dynamics in Multisublattice Magnets. *Phys. Rev. Lett.* **108**, 057202 (2012).
- 12. Schellekens, A. J. & Koopmans, B. Microscopic model for ultrafast magnetization dynamics of multisublattice magnets. *Phys. Rev. B* **87**, 020407 (2013).

- 13. Medapalli, R. *et al.* Efficiency of ultrafast laser-induced demagnetization in Gd_xFe_{100-x-y}Co_y alloys. *Phys. Rev. B* **86**, 054442 (2012).
- 14. Johnsen, P. C. *et al.* A beamline for ultrafast extreme ultraviolet magneto-optical spectroscopy in reflection near the shot noise limit. *Rev. Sci. Instrum.* **94**, 033001 (2023).
- 15. El Idrissi, B. C., Venturini, G., Malaman, B. & Fruchart, D. Magnetic structures of TbMn₆Sn₆ and HoMn₆Sn₆ compounds from neutron diffraction study. *J. Common Met.* **175**, 143–154 (1991).
- 16. Shi, X. *et al.* Ultrafast electron calorimetry uncovers a new long-lived metastable state in 1T-TaSe2 mediated by mode-selective electron-phonon coupling. *Sci. Adv.* **5**, eaav4449 (2019).
- 17. Pankratova, M. *et al.* Heat-conserving three-temperature model for ultrafast demagnetization in nickel. *Phys. Rev. B* **106**, 174407 (2022).
- 18. CXRO The Center for X-ray Optics. https://cxro.lbl.gov/.
- 19. Stöhr, J. & Siegmann, H. C. *Magnetism: From Fundamentals to Nanoscale Dynamics*. vol. 152 (Springer, Heidelberg, Germany, 2006).
- 20. Chubykalo-Fesenko, O., Nowak, U., Chantrell, R. W. & Garanin, D. Dynamic approach for micromagnetics close to the Curie temperature. *Phys. Rev. B* **74**, 094436 (2006).
- 21. Lyberatos, A. & Guslienko, K. Y. Thermal stability of the magnetization following thermomagnetic writing in perpendicular media. *J. Appl. Phys.* **94**, 1119–1129 (2003).
- 22. Sato, M. & Ishii, Y. Simple and approximate expressions of demagnetizing factors of uniformly magnetized rectangular rod and cylinder. *J. Appl. Phys.* **66**, 983–985 (1989).

Supplementary Materials

Model Equations

While the demagnetizing field, $\mathbf{H_{demag}}(t)$, is much weaker than the anisotropy field, we still included an approximation of the demagnetizing field in the model. To calculate the demagnetizing field, we approximated the sample as a cylinder. The height of the sample was 0.7 mm and the diameter was 3.3 mm at its widest and 1.9 mm at its narrowest. We approximated this as a cylinder with a diameter four times its height. We then used an approximation²² for the demagnetizing factors to obtain a demagnetizing field of:

$$\mathbf{H_{demag}}(t) = \begin{pmatrix} -0.18 \, M_x(t) \\ -0.18 \, M_y(t) \\ -0.64 \, M_z(t) \end{pmatrix} \tag{S1}$$

where $M_{x,y,z}$ are the components of the magnetization projected along different axes. These are calculated from projects of the instantaneous $\mathbf{m}(t)$ multiplied by the temperature-dependent saturation magnetization M_S . The saturation magnetization depends on the temperature of the spin system, which in itself depends on time. Therefore, we write M_S as: $M_S\left(T_{\mathrm{spin}}(t)\right)$.

The saturation magnetization is calculated based on the temperature-dependent Mn and Tb moments:

$$M_s(T_{\rm spin}) = \left(6\mu_{\rm Mn}(T_{\rm spin}) - \mu_{\rm Tb}(T_{\rm spin})\right)/V. \tag{S2}$$

The Tb moment per atom, $\mu_{\mathrm{Tb}}(T_{\mathrm{spin}})$, is subtracted due to its ferrimagnetic alignment with Mn. The Mn moment per atom, $\mu_{\mathrm{Mn}}(T_{\mathrm{spin}})$, is multiplied by 6 as there are 6 Mn atoms per unit cell. The temperature-dependent Tb and Mn magnetic moments come from neutron scattering data from El-Idrissi $et~al.^{15}$ This total moment is then divided by the volume of the unit cell, V, to convert to total magnetization. V is calculated based on the unit cell vectors given by Jones $et~al.^4$, i.e. $V=a^2c$ where a = 5.538 Å and c = 9.0326 Å

We calculate the anisotropy field, $\mathbf{H_{anis}}(t)$, using the element-specific, temperature-dependent, magnetic anisotropy energies, MAE_{Tb} and MAE_{Mn} , as described by Jones *et al.*⁴ $\mathbf{H_{anis}}(t)$ drives the temperature-dependent dynamics and is given by the following expression:

$$\mathbf{H_{anis}}(t) = \begin{pmatrix} 0 \\ 0 \\ m_z(t) \left(\frac{MAE_{\mathrm{Tb}} \left(T_{\mathrm{spin}}(t) \right)}{\mu_0 M_s \left(T_{\mathrm{spin}}(t) \right)} + \frac{6MAE_{\mathrm{Mn}} \left(T_{\mathrm{spin}}(t) \right)}{\mu_0 M_s \left(T_{\mathrm{spin}}(t) \right)} \right) \end{pmatrix}$$
 (S3)

The factor of 6 in the expression for Mn accounts for the six Mn atoms per cell.

Changing the Model Temperature Profile

Since the exact shape of the time-dependent spin temperature profile is unknown, Figs. S1 (b)-(f) simulate different parameters for the applied temperature profile based on Eq. 6. The effect of changing the incident fluence is shown experimentally in Fig. S1(a), and in simulation in Fig. S1(b), as displayed in the main text, Fig. 5. The parameters tested include the ratio of the amplitudes of the fast and slow spin

temperature decay, A_2 and A_3 , as well as the timescales themselves. Unless otherwise specified in the subfigure legends of Fig. S1, the parameters used were the same as in the main text: $T_0 = 270$ K, $A_2 = 1/2$ A_1 , $A_3 = 1/2$ A_1 , $\tau_{\rm rise} = 1$ ps, $\tau_{\rm decay1} = 3$ ps, $\tau_{\rm decay2} = 200$ ps, and $\alpha = 1$. Additionally, $A_1 = 35$ K. There is good agreement across a wide range of temperature model parameters shown in Fig. S1. In the simulations in Fig. 5, a damping of $\alpha = 1$ was used. More physical values of α (e.g. 0.01 to 0.1), are depicted in Fig. S1(h). The overall envelope of the rise and decay is similar for each damping factor.

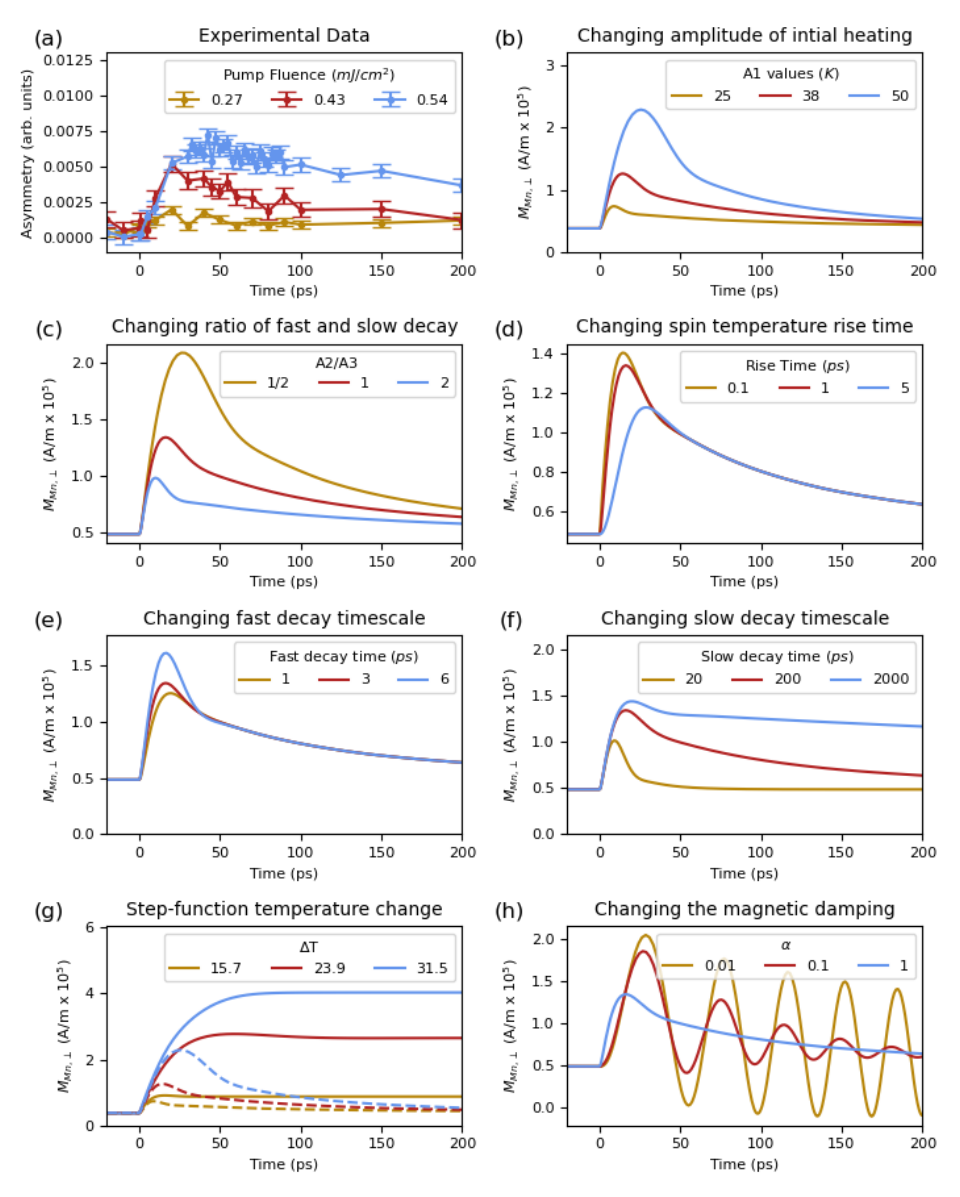


Figure S1. A low fluence dynamic model of Tb166. The modeling is based on the temperature profile described by Eq. 6. Experimental data is presented for comparison in (a). The effects of changing the model parameters are shown. These are: (b) changing the amplitude of the initial heating A_1 ; (c) changing the ratio of the amplitudes of the fast and slow temperature decays, A_2 and A_3 ; (d) changing the rise time of the spin bath temperature, τ_{rise} ; (e) changing the fast decay timescale, τ_{decay1} ; and (f) changing the slow decay timescale, τ_{decay2} . In (g), a step-function temperature change is used instead of a three-exponential model. ΔT values are chosen to match the maximum temperature changes from subfigure (b) and the data from subfigure (b) is overlaid as dotted lines. In (h), the magnetic damping factor, α , is varied.

In Fig. S1(g) the laser-induced temperature change is modeled as a step-function. No exponential increases or decreases were applied, instead an instantaneous ΔT was introduced at t = 0. The purpose of investigating the temperature step-function was to isolate the effects of the model-specific rise times and decays from the system's intrinsic spin-reorientation timescale. The data from subfigure (b) is overlaid on (g) as dotted lines. The maximum temperature changes induced by the A_1 in subfigure (b) were used to set the ΔT values for the step-function model. In the case of ΔT = 15.7 K, a partial reorientation takes place, as seen in subfigure (g). In the case of ΔT =23.9 K or 31.5 K, full reorientations occur.

Modeling the High Fluence Data

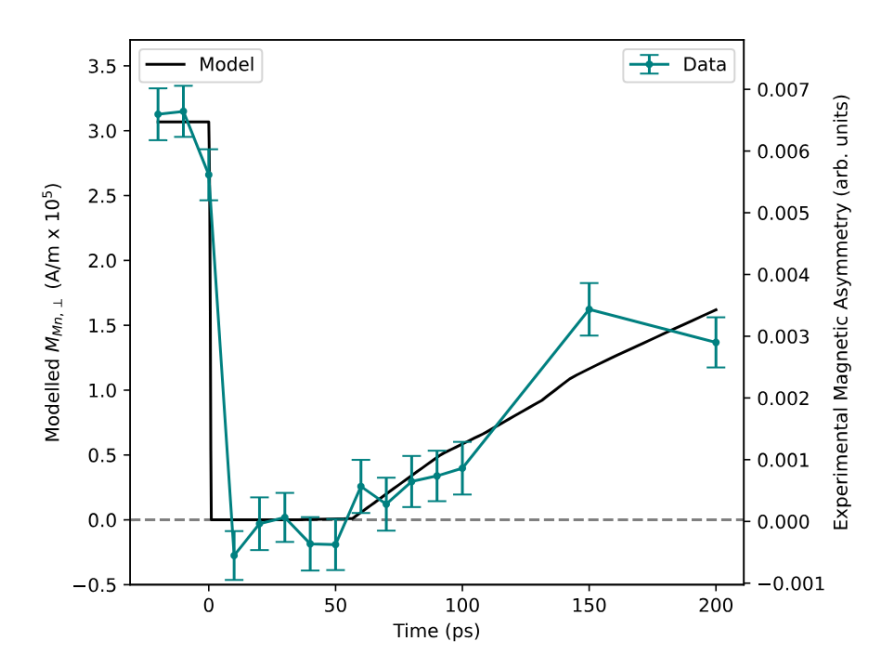


Figure S2. Modeling the high fluence behavior of Tb166. The model utilizes an initial temperature of 294 K, an A_1 amplitude of 275 K, and a slow decay time constant of 800 ps. The experimental data is for a fluence of 3.6 mJ/cm².

For the highest fluence experimental data, 3.6 mJ/cm² and 2.1 mJ/cm², all measurements after t = 0 are above T_{SR} so there are no reorientations. In this case, the LL or LLB equations are not required as there is no precessional motion to be modeled. The dynamics in the high fluence section are treated purely in terms of the change in M_S as a function of changing sample temperature.

The experimental data from a fluence of 1.1 mJ/cm^2 is more difficult to model because, in this case, the sample passes through T_C on early timescales then reaches T_{SR} on longer timescales. Therefore, measurements are in the regime of T_C and will also require a precessional model for the near T_{SR} behavior. This data would be best modeled with the LLB equation and so we omit its treatment as it is beyond the scope of this work.

In Fig. S2, the experimental data for 3.6 mJ/cm² is plotted. A three-exponential temperature model is applied. For the model, a larger initial sample temperature (294 K) was used compared to the low fluence modeling (270 K) as the initial in-plane signal was larger for the high fluence data. The slow decay time

was increased to 800 ps to match the experimental results, and the A_1 amplitude was increased to 275 K (note that 3.6 mJ/cm² is 6 times larger than the largest experimental fluence in the low fluence results). The increase in the slow decay timescale is understandable as there are many competing timescales for heat transport in the sample and it may be more difficult for a sample to dissipate additional heat when the baseline temperature of the sample is hotter.

Definition and Measurement of the Normalization Factor

The measurements in Fig. 2 took between 16 and 24 hrs of data collection per fluence to achieve the signal-to-noise ratio presented. One issue associated with taking data over these long timescales was sample damage induced by the pump and probe lasers. The sample was very small (few mm's diameter) and, in many areas, the surface roughness was too large to make a measurement. Therefore, we were limited to taking data in one sample location per fluence. The pump pulses were a low energy (≈1.59 eV), high fluence (few mJ/cm² range) source of damage, while the probe laser has a comparatively much lower fluence (four orders of magnitude lower) but significantly higher photon energy (30 -73 eV range). The sample damage reduced the magnetic signal over time. To prevent sample damage from influencing the measured dynamic behavior, the order in which the time points were measured was randomized. This random order was then repeated hundreds of times. This prevented systematic errors that would arise when measuring the time points sequentially. Nonetheless, the sample damage reduced the overall amplitude of the signal. The amount of damage differed between different pump fluences and sample locations.

After taking the original data with 6 fluences on 6 different sample locations, we devised a normalization procedure to allow us to compare the magnitudes of signals obtained despite sample inhomogeneities and fluence dependent damage from the pump laser. We called this the normalization factor, denoted (NF). The NF is calculated in Table 1 and applied to all the data in Figs. 2, 3 & 4. The steps used to determine the NF value are described below.

The measurement of the NF was made after the original 16-24 hr scans of varying fluence depicted in Fig. 2. The sample locations used for the original scans were already highly damaged. Therefore, we chose 6 new high reflectivity, undamaged locations on the sample for the NF measurement. These 6 sample locations were used to determine the NFs for the 6 fluences used in the study and appear in Table 1, column 1. The measurement of the NF consisted of two steps: the CV measurement and the MV measurement.

The first step is the control value (CV) measurement. To obtain the CV, we measured the magnetic signal with 0.54 mJ/cm² pumping, taken at a fixed pump-probe delay (30 ps). The fluence of 0.54 mJ/cm² was chosen because it induces a well-defined magnetic response without excessive sample damage. The time delay of 30 ps was chosen as this is where the signal is largest for 0.54 mJ/cm² pumping. By measuring each new sample location under the same conditions, we determined the severity of sample inhomogeneities and attempted to mitigate their influence. We calculated the mean of the six measurements and use this to normalize each CV measurement. The normalized CV values are depicted in column 2 of Table 1. The maximum deviation from the mean was 20%. i.e. CV=1.2 (at location 2).

The second step is the measurement value (MV) measurement. The MV is obtained by measuring the MOKE signal for each of the six fluences with a pump-probe delay chosen to maximize the signal. Each fluence is measured on a different one of the six sample locations from the CV measurement. The time delays for the MV measurements were chosen to maximize the signal for each specific fluence. The chosen

time delays were: 20 ps, 30 ps, 30 ps, 70 ps, 200 ps, and -10 ps respectively. The MV values are listed in Table 1, column 4. Unlike the CV values, the MV values across different sample locations should not be similar to each other as they were taken at different fluences and different time delays.

Sample	Control	Fluence	Measured	Value in	Normalization
Location	Value	(mJ/cm²)	Value	Real Data	Factor
Location	CV		MV (1e-3)	RV (1e-3)	NF = (MV / RV)
	CV		IVIV (1e-5)	NV (16-3)	*1/CV
<u> </u>					
1	0.96 ± 0.17	0.27	1.9 ± 0.9	2.5 ± 0.3	0.8 ± 0.4
2	1.20 ± 0.22	0.43	4.8 ± 1.1	2.9 ± 0.4	1.4 ± 0.4
3	1.00 ± 0.17	0.54	5.7 ± 0.9	4.1 ± 0.3	1.4 ± 0.3
4	0.96 ± 0.15	1.1	9.0 ± 0.8	5.2 ± 0.4	1.8 ± 0.3
5	0.00 ± 0.15	2.1	8.4 ± 0.9	47+04	1.8 ± 0.4
3	0.98 ± 0.15	2.1	8.4 ± 0.9	4.7 ± 0.4	1.0 ± 0.4
6	0.90 ± 0.20	3.6	6.0 ± 1.0	5.8 ± 0.4	1.1 ± 0.3

Table 1: Calculations of the normalization factors used for each fluence. Error bars in the CV, MV, and RV represent the standard error based on repeated measurements. The errors in NF are calculated using standard error propagation techniques. Error on the NF is not represented in the error bars on figures in the main text.

Before both the CV and MV measurements, the sample had to thermalize with the relevant pump fluence so that the temperature of the sample would be stable throughout the scan. The probe was blocked while thermalizing with the pump (to limit sample damage from EUV). Furthermore, we kept each measurement as short as possible to limit sample damage. The timing was as follows: thermalize for 35 mins with 0.54 mJ/cm², measure the CV for 1 hour, thermalize for 15 mins with chosen fluence, measure the MV for 1 hour. These timings were a trade-off between improving signal-to-noise and minimizing exposure to the laser beams.

Finally, in Table 1, column 5, we recorded the measured asymmetries from the full dynamic fluence-dependent traces at the same specific fluences and time delays used for the MV. These values are the real values (RVs). The RVs give us information on how much the measured signal was reduced due to sample damage over a long scan compared to the relatively short MV scans. By combining the values of the CV, MV and RV, the normalization factor can be calculated using the formula in Table 1, column 6.

For all fluences, except 0.27 mJ/cm², the normalization factor was greater than 1, i.e. the normalization process increased the magnitude of the signal. An NF>1 is expected in order to compensate for sample damage that occurs over the dynamic scans. The reason the 0.27 mJ/cm² fluence NF was not >1, may be because it had the least pumping, and therefore the least sample damage. Furthermore, the error bars on the 0.27 mJ/cm² NF were quite large due to the small overall magnetic signal induced by this fluence.